Linearized Navier-Stokes Analysis for Rotor-Stator Interaction Tone Noise Prediction

Anupam Sharma*, Hsuan-nien Chen†, and Chingwei M. Shieh‡

Computational Heat Transfer & Aeroacoustics Laboratory,

Energy and Propulsion Technologies,

General Electric Global Research Center, One Research Circle, Niskayuna, NY, 12309, USA

Tonal noise due to aerodynamic interaction between turbomachinery blade rows has been conventionally studied using time-linearized, inviscid analyses. While the perturbation equations can employ the inviscid flow approximation, the meanflow calculation has to be viscous to capture the loading distribution on the blades. In a previous study, the authors suggested calculating approximate inviscid meanflow with a "comparable" loading distribution. Experience has shown that this can not only be tedious but also can introduce large variations in predictions. Therefore, a linearized RANS calculation is proposed to replace the linearized Euler calculation. Validation of the approach is performed against semi-analytical solutions of canonical problems, and comparisons against NASA Source Diagnostic Test (SDT) data are presented. It is shown that the geometric trends are reasonably well captured with the approach although no clear improvement in prediction accuracy is observed in comparison to the inviscid approach. Detailed comparisons of predicted rotor wake harmonics against Laser Doppler Velocimetry (LDV) data are also presented.

Nomenclature

$a_{m,n}$	Complex amplitude of the (m,n) mode
c	Speed of sound
k_z	Complex wave number in axial direction
m	Circumferential mode number
n	Radial mode number
N_B	Number of rotor blades
N_V	Number of stator vanes
r_H	Hub radius
r_T	Tip radius
$\mathrm{P_{ref}}$	Reference acoustic pressure = 20 μPa
$\mathrm{PWL_{ref}}$	Reference acoustic power = 10^{-12} watts

Symbols

Ω	Rotor shaft rotation rate (rad/s)
ϕ	Phase of a complex variable
$\psi_{m,n}$	Eigenvector corresponding to the (m,n) mode
$\sum$	Sum of radial mode power levels

Superscripts

(a)	$\overline{\rho^{-1}}\,(p' + \overline{\rho}\,\overline{v}_z v'_z)$
(b)	$\overline{\rho} v'_z + \rho' \overline{v}_z$

*Mechanical Engineer, K1 2C-25A, sharma@ge.com, AIAA Member

†Mechanical Engineer, K1 2C-35, chen@ge.com, AIAA Member

‡Fluid Mechanics Engineer, K1 2C-37A, shieh@ge.com, AIAA Member

I. Introduction

ROTOR-stator interaction tone noise is a community noise concern for high-bypass ratio aircraft engines, especially at approach. This noise source is often referred to as "fan tone noise" and will be abbreviated to FTN in this paper. FTN is the result of periodic interaction between the viscous rotor wakes and downstream stators. This interaction converts vortical energy in the wake to acoustic energy, which then propagates out from the inlet and exhaust of the engine. The upstream propagating wave interacts with the rotor that impedes and scatters the acoustic wave; the downstream propagating wave however transmits relatively unimpeded and radiates out of the exhaust. This paper primarily addresses the exhaust radiated fan tone noise.

Several fan tone noise prediction methodologies have been developed in the last few decades. These methods include - classical semi-analytical methods, unsteady linearized perturbation (forced/gust response) analysis, and non-linear time-marching computational aeroacoustics (CAA) methods. This paper uses unsteady linearized perturbation analysis for FTN prediction.

This work follows previous work by the authors (see Sharma *et al.*[1]) where linearized Euler analysis was employed. The previous approach involved computation of "representative" inviscid stator (OGV) meanflow over which linearized perturbation analysis could be carried out. This procedure involved cumbersome iterations in an attempt to efficiently match the inviscid OGV meanflow to the viscous meanflow. This made the process time consuming as well as user-dependent, as there is no consistent metric to define a suitable match between the two (viscous and inviscid) physically different meanflows. The current procedure uses linearized Navier-Stokes analysis instead of linearized Euler analysis. The linearized perturbation analysis is carried out over viscous meanflow solution, thus removing the inviscid meanflow calculation/matching step from the process. This also eliminates the need for "idealizing" the wake that was required in the prior process to conform to the inviscid meanflow.

The new process is validated against semi-analytical solutions for canonical problems as well as experiment data, using results from the Source Diagnostic Test (SDT) conducted at NASA Glenn. Comparisons against data are shown for rotor wakes (measured using LDV) and for acoustic power measurements made using a rotating rake. For brevity, the following abbreviations will be used heretofore: IFTN to refer to the inviscid analysis and VFTN to refer to the present viscous analysis.

Section II describes the proposed VFTN prediction procedure. The validation studies against canonical test cases and comparisons against test data are reported in section III.

II. Noise Prediction Process

Fig 1 shows a flowchart of the VFTN prediction process, which consists of the following five steps:

1. Viscous meanflow computation for rotor and stator/OGV
2. Convection of the rotor wake from the rotor trailing edge to the OGV leading edge.
3. Wake extraction from rotor mean flow solution
4. Linearized viscous perturbation simulation
5. Extraction of acoustic in-duct pressure and power levels.

The first step is the computation of the viscous mean flows for both the rotor and the stator. Reynold's Averaged Navier-Stokes (RANS) analyses using a $k-\omega$ turbulence model are carried out in the frame fixed to the rotor and stator respectively. A highly converged meanflow for the stator (OGV) is desirable as any numerical residual will act as a forcing function (source) in the linearized simulation.

The second step involves solving RANS equations in the rotor frame of reference to convect the rotor wakes from the rotor trailing edges to the OGV leading edges. One could use a parabolic solver as only the downstream convected disturbance needs to be modeled, however, the RANS solver is used here. This "extra" step is performed for two reasons: firstly, it permits a mesh that can follow the wake so that the mesh density can be increased in the free shear (high gradients) region for reducing numerical discretization errors; secondly, it permits the placement of the exit boundary of the domain far downstream of where the wake harmonics are extracted (at the inlet of the OGV computation domain). This reduces the impact of any reflections on the wake harmonics from the exit boundary of the domain; the non-reflecting boundary

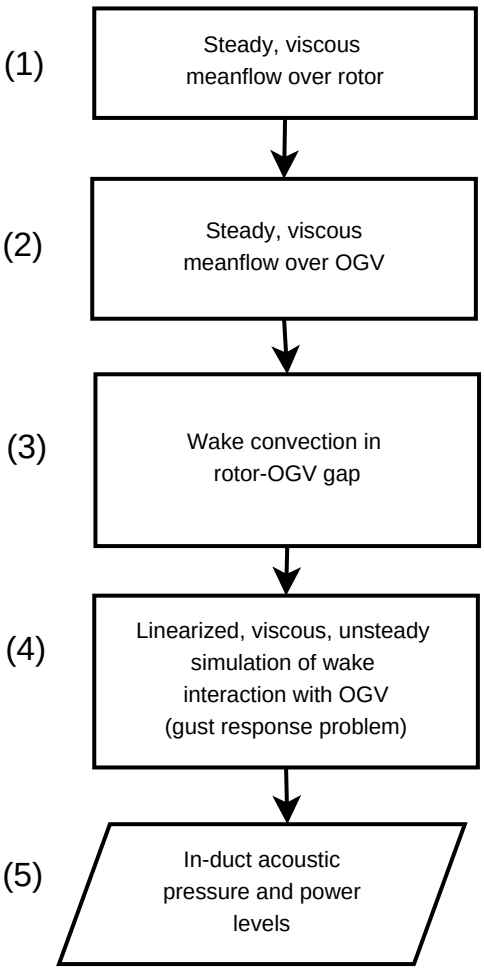

Figure 1. A flowchart of the VFTN prediction process.

conditions due to Giles[2] are employed, however small reflections are expected in a highly 3-dimensional flow as is the case here. Fig. 2 qualitatively exemplifies the benefit of aligning the wake and clustering the region of high flow gradients in the wake for the same total grid size. The numerical smearing of the wake can be clearly seen to be higher in the axial grid case.

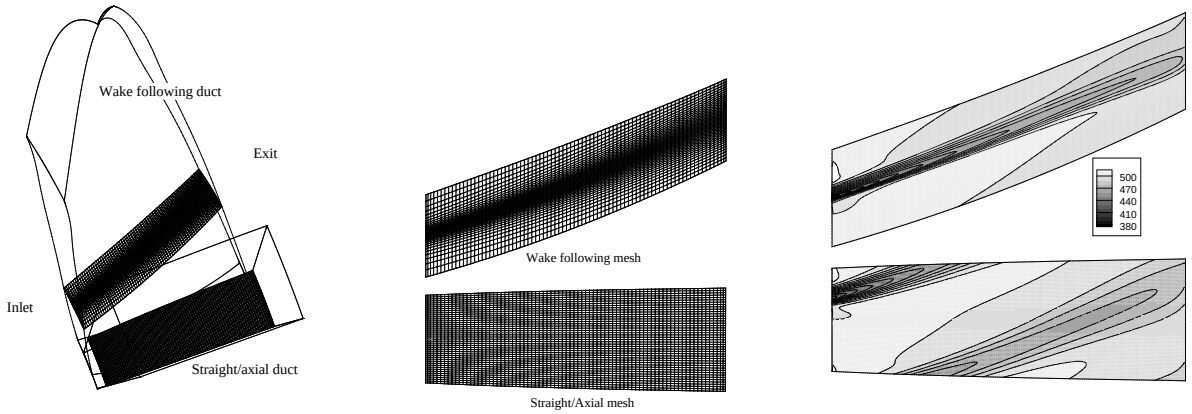

(a) 3-D Outline (b) Mesh (c) Absolute total velocity contours

Figure 2. Comparisons of straight/axial duct/mesh against a wake-following duct/mesh. (a) 3-D outline, (b) mesh at a constant radius location, and (c) absolute total velocity contours on the constant-radius plane.

In the third step, temporal harmonics of the rotor wake are computed from the solution obtained in step two. These are computed from the RANS solution by performing a spatial (circumferential) Fourier transform of the solution. For a constant rotor rotation rate, a circumferential Fourier transform in the rotor frame of reference is equivalent to a temporal Fourier transform in the stationary frame. Previous IFTN analysis also required "idealization" of the rotor wake near the hub and tip casing boundaries to be compatible with the linearized inviscid analysis. This undesirable and rather arbitrary step has been removed from the current VFTN analysis.

The fourth step is the linearized viscous perturbation computation. The harmonic representation of the wake profile is applied as a perturbation at the OGV inlet boundary for the linearized calculation. This perturbation is convected downstream by the mean flow where it interacts with the OGVs generating upstream and downstream propagating acoustic waves. A 3D acoustic mode decomposition is performed at the exit boundary of the computational domain and the sound pressure and power levels for each downstream propagating acoustic mode are calculated. A 3-D non-reflecting boundary condition described in reference[1] is used for the linearized analyses. This boundary condition decomposes the perturbation field at the exit boundary into incoming and outgoing waves. The outgoing and non-decaying acoustic modes are then used (in step 5) along with equations (1) and (2) to calculate the outgoing acoustic integrated sound pressure (SPL) and power (PWL) levels:

$$\mathrm{SPL} = 10\,\log_{10}\left(\frac{1}{r_T^2 - r_H^2}\sum_{m,n}|a_{m,n}|^2\int_{r_H}^{r_T}|\psi_{m,n}|^2\,r\,\mathrm{d}r\right) - 10\,\log_{10}(P_{\mathrm{ref}}^2), \tag{1}$$

where r_H and r_T are the hub and tip radii of the annular duct, m and n are respectively the circumferential and radial numbers of the propagating acoustic modes, $\psi_{m,n}$ and $a_{m,n}$ are the eigenmode and the mode amplitude, respectively, corresponding to the (m,n) mode, and $P_{\mathrm{ref}} = 20$ μPa is the reference acoustic pressure.

$$\mathrm{PWL} = 10\,\log_{10}\left(\pi Re\left\{\sum_{m,n}|a_{m,n}|^2\int_{r_H}^{r_T}\psi_{m,n}^{(a)}(\psi_{m,n}^{(b)})^*\,r\,\mathrm{d}r\right\}\right) - 10\,\log_{10}(\mathrm{PWL}_{\mathrm{ref}}), \tag{2}$$

where $\psi_{m,n}^{(a)}$ and $\psi_{m,n}^{(b)}$ are the eigenmodes corresponding to the quantities $\overline{\rho^{-1}}\,(p' + \overline{\rho}\,\overline{v}_z v_z')$ and $\overline{\rho}v_z' + \rho'\overline{v}_z$ respectively, and $\mathrm{PWL}_{\mathrm{ref}} = 10^{-12}$ watts is the reference power level. Note that the summation in equations (1) and (2) is performed over the propagating acoustics modes only.

III. Process Validation

Validation is performed against semi-empirical solutions for canonical cases and against wind tunnel test data. Two semi-empirical canonical cases are selected. The canonical cases selected here were previously validated[1] with the IFTN analysis hence only a subset of cases are tested for verification purposes. Results from the Source Diagnostic Test (SDT) conducted at the National Aeronautics and Space Administration (NASA) Glenn $9' \times 15'$ Low Speed Wind Tunnel are used for experimental validation.

A. Canonical Cases

In this section, validation of the prediction process against semi-analytical results for two benchmark problems[3,4] is presented. The interaction of a vortical gust with a flat plate cascade is solved in two and three spatial dimensions to predict the unsteady loading on the blades. The benchmark problems assume inviscid flow, however the base flow in the numerical simulation here is treated as viscous. An infinitesimal thickness is added to the flat plate to avoid the leading edge singularity. Zero velocity is enforced at the wall.

The gust may be represented generally by

$$\mathbf{v}' = \sum_{n=1}^{\infty} \mathbf{v}'_{\mathbf{n}} \exp\left\{i\, n\, N_B \left(-\Omega t + k_z z + \theta + \phi\right)\right\}, \tag{3}$$

where N_B is the number of rotor blades, Ω is the shaft rotation rate, ϕ is the phase, and n is the harmonic number. For a gust convecting with a uniform meanflow velocity $\overline{v}_z$, the axial wave number, $k_z = \Omega/\overline{v}_z$. The radial dependence of the gust must satisfy the solenoidal constraint $\nabla.\mathbf{v}' = 0$. Following Prasad and Verdon,[5] the gust is defined as

$$\left(v'_{n_r}, v'_{n_\theta}, v'_{n_z}\right)^T = a_n \overline{v}_z \left(0, 1, -\frac{\overline{v}_z}{\Omega r}\right)^T, \tag{4}$$

$$\left(v'_{n_r}, v'_{n_\theta}, v'_{n_z}\right)^T = a_n \overline{v}_z \left(0, 1, -\frac{\overline{v}_z}{\Omega r}\right)^T, \tag{5}$$

where a_n is the complex amplitude of the gust and Ω is varied by changing the tip Mach number, $M_t = \Omega r_T/c$ of the rotor, where r_T is the tip radius and c is the speed of sound. The rotor and stator blade counts, N_B and N_V respectively, determine the inter-blade phase angle, $\sigma = -2\pi n N_B/N_V$. Only the $n = 1$ case is presented here and the parameter values are listed in Table 1.

Table 1. Parameters for flat plate cascade validation

Parameter		Value
N_B	=	16
N_V	=	24
$\overline{v}_z$	=	1.0
c	=	2.0
n	=	1
a_1	=	1

1. *Gust Response of a 2-D Flat Plate Cascade*

A narrow annulus flat plate cascade is used to approximately simulate a 2-D case for comparison against results from Smith's[6] analysis. The hub-to-tip ratio for the simulated geometry is 0.98, and $M_t = 0.6495$. Figure 3 compares the imaginary part of unsteady pressure in the cascade and Figure 4 compares the unsteady lift on the cascade. The agreement between the numerical results and Smith's results[6] is excellent.

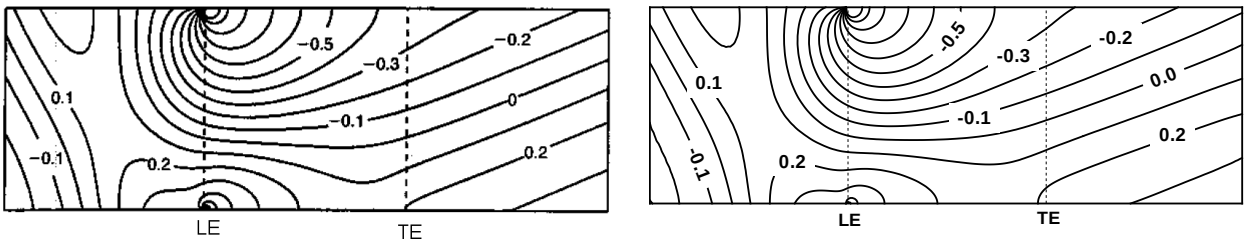

(a) Classical (b) Numerical

Figure 3. Contours of imaginary part of unsteady pressure: (a) Classical results,[6] and (b) VFTN numerical results.

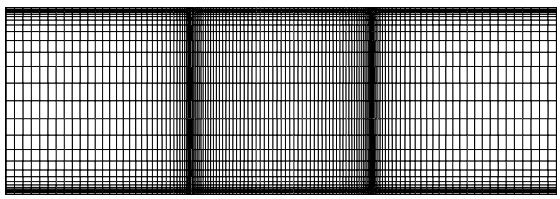

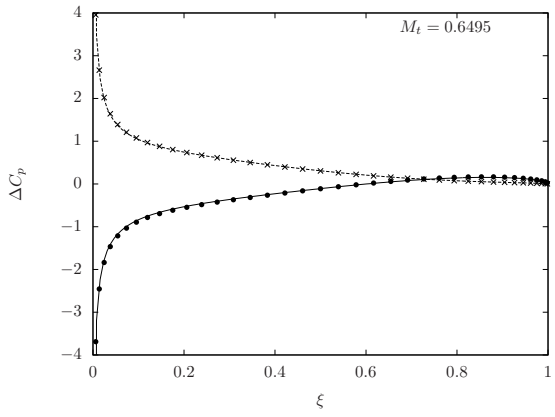

(a) (b)

Figure 4. (a) Grid and (b) unsteady lift on a 2-D flat plate cascade for $M_t = 0.6495$. Lines are predictions and symbols are classical results by Smith.[6]

2. Gust Response of a 3-D Flat Plate Cascade

For the 3-D flat plate cascade response problem, the tip radius is 3.8197, hub to tip radius ratio is 0.5, and $M_t = 0.783$. Semi-analytical results for this case were presented by Namba and Schulten.[8] Figure 5 presents a comparison of the unsteady lift on the blade at the mid-span location. The results are in good agreement with the semi-analytical results.

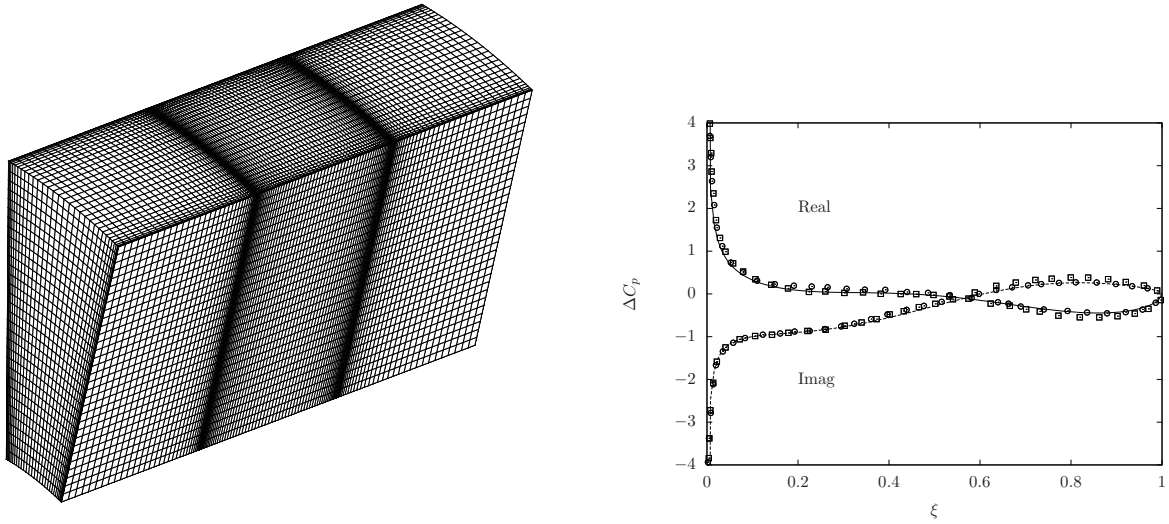

(a) Grid (b) Unsteady lift

Figure 5. (a) Grid and (b) unsteady lift at mid-span location of a 3-D flat plate cascade. Lines are predictions, filled circles are results from Namba, and squares are results from Schulten.[8]

B. Source Diagnostic Test Data Comparison

The Source Diagnostic Test (SDT) is a comprehensive experimental study of the aerodynamics and acoustics of a representative high bypass-ratio fan stage. One of the goals of the SDT study was to determine the factors affecting the generation of fan tone noise due to the interaction of the fan rotor wakes with the outlet guide vanes. Aerodynamic and acoustic measurements were taken for various rotor and stator geometry configurations and operational speeds. Two rotor and three stator geometries were tested in the SDT. The three stator geometries were nominal (NOM), low vane count (LVC), and low noise (LN) (see Fig. 6). The design parameters for the rotor and stator are outlined in Table 2 and Table 3 respectively. The rotor speed parameters are outlined in Table 4.

Table 2. Rotor design parameters

Rotor	No. Blades	L.E. Sweep	Design Tip Speed (ft/sec)	Pressure Ratio
R4	22	0	1215	1.47
M5	22	0	1350	1.50

Table 3. Stator design parameters

Stator	No. Vanes	L.E. Sweep	Aspect Ratio	Solidity
Nominal (NOM)	54	0	3.51	1.52
Low Vane Count (LVC)	26	0	1.67	1.51
Low Noise (LN)	26	30	1.67	1.53

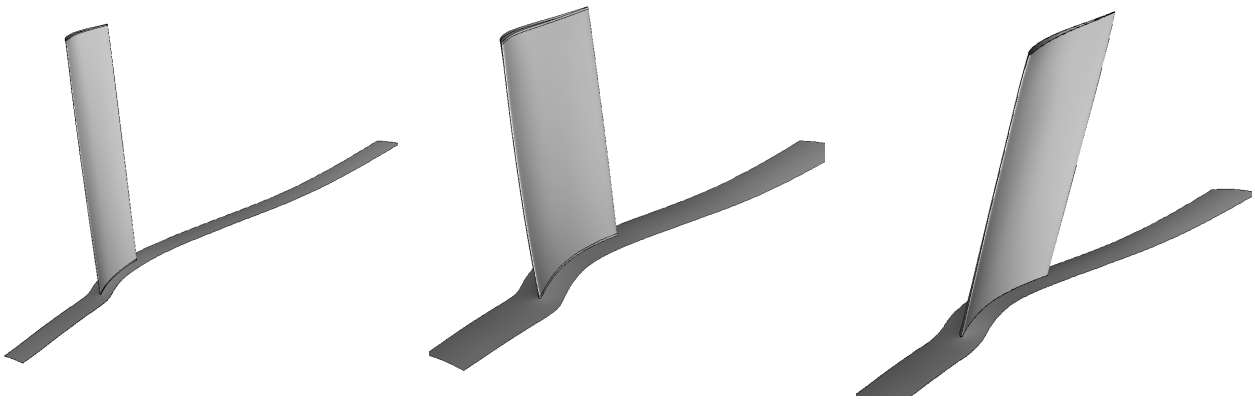

(a) NOM (b) LVC (c) LN

Figure 6. The three stator geometries tested in SDT: (a) 54 blade count nominal stator, (b) 26 blade count radial stator, and (c) 26 blade count swept stator.

Table 4. Rotor speed parameters

Condition	RPM (Corrected)	Percent Speed	Tangential Tip Speed (Corrected) (ft/sec)
Approach	7809	61.7	750
Cutback	11075	87.5	1063
Takeoff	12657	100	1215

A subset of the experimental results was selected to validate the present prediction method. This included the R4 rotor with all three stator configurations. For each stator configuration, calculations were performed for approach, cutback and takeoff rotor speeds and at the first and second blade passing frequencies. This gives a total of 16 cases (the nominal stator is cut-off at first BPF except at takeoff condition). These are listed in Table 5. Comparisons against measured data are made for: (a) circumferentially averaged velocity profiles, (b) rotor wake harmonics, and (c) in-duct modal sound power for first two blade passing harmonics.

1. Comparisons Against LDV Data

LDV measurements were made at two axial locations between the fan blades and the OGVs. In this section comparisons are made for the data collected at the first axial station (0.81 rotor tip chord downstream of the rotor trailing edge). The streamwise and cross-stream velocity components were measured. Comparisons between predictions and data are made for circumferentially averaged axial and circumferential velocity components in Fig. 7. The differences between data and prediction are not insignificant and are of the order of 3%. Unfortunately, at the time these runs were carried out, radial profiles of total pressure and temperature conditions were not available, and the authors had to use radial equilibrium assumption with the 1-D area-averaged massflow and pressure ratio results from the measured fan performance map. It appears that for the approach condition, even the area averaged numbers between CFD and LDV data would be different as the CFD consistently overpredicts the axial velocity and underpredicts the swirl velocity. This suggests that the rotor and stator incidence angles in CFD are slightly inconsistent with the test data. The match is expected to be better if radial profiles were specified for the meanflow calculations.

In order to facilitate comparisons of the wake harmonics, a co-ordinate system aligned with the relative streamwise flow direction is used. In Fig. 8, this co-ordinate system is defined by the axes ζ and η, where ζ is in streamwise direction, and η is in the cross-stream direction. One advantage of using this co-ordinate system is that the viscous wake deficit is primarily along the ζ direction, and hence comparing the ζ component of the wake deficit is sufficient.

Although it is physically more intuitive to plot wake defect as a function of θ (in the rotor frame of reference), our interest is in tone noise at the first few rotor blade passing harmonics. Hence comparisons

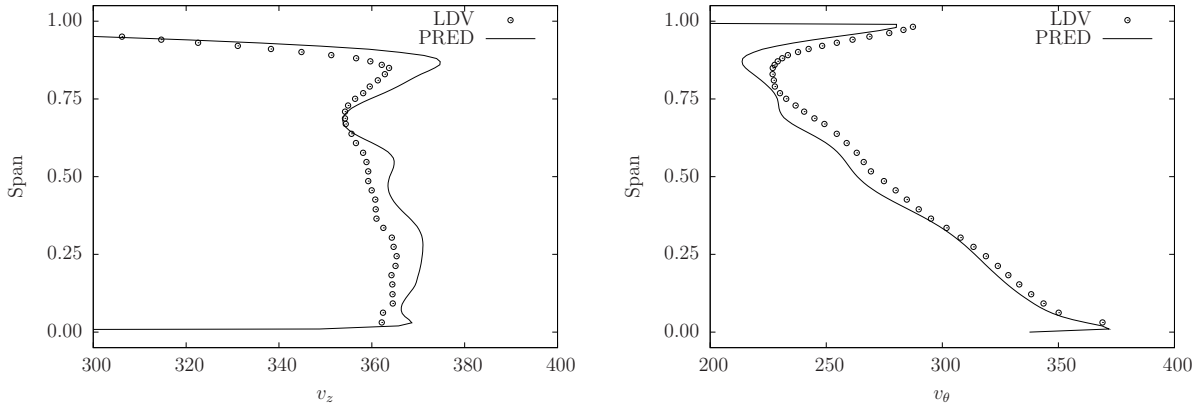

(a) Approach

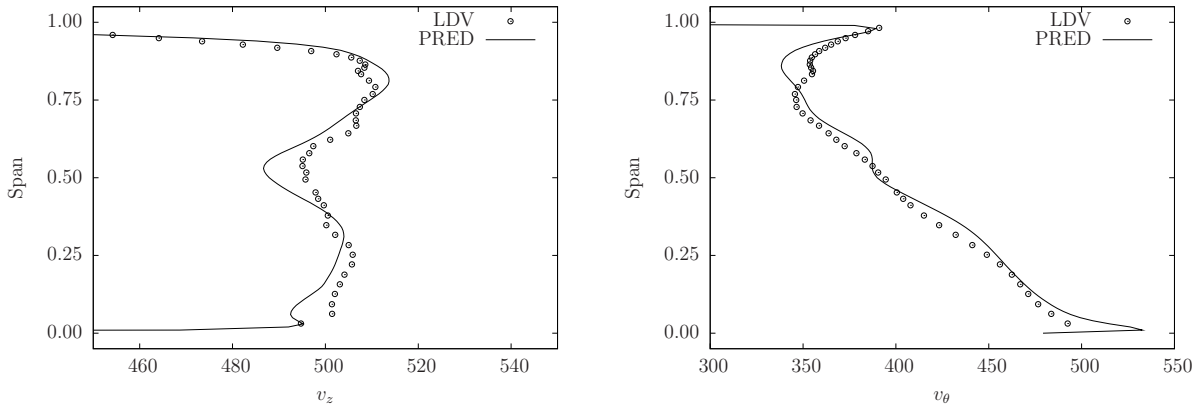

(b) Cutback

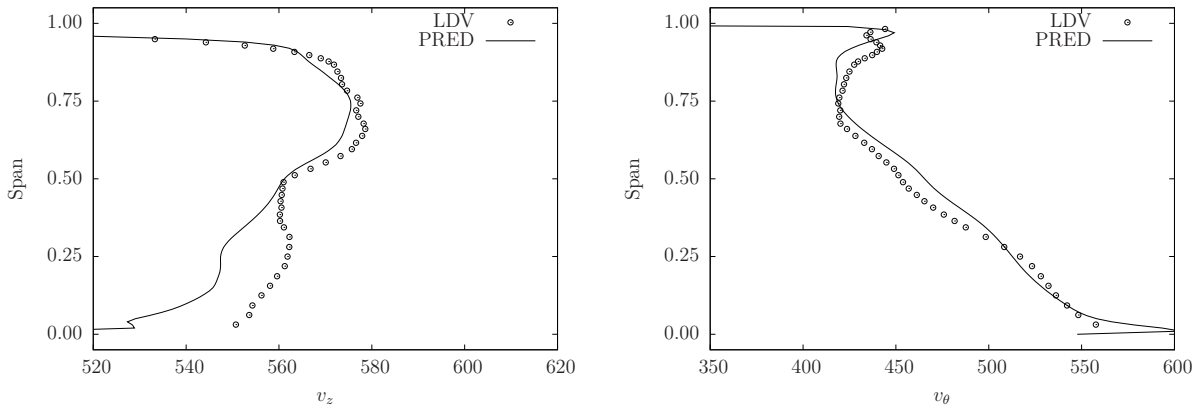

(c) Takeoff

Figure 7. Circumferentially averaged meanflow (axial, v_z and tangential, v_θ) comparisons with LDV data at an axial distance of 0.81 rotor tip chord downstream of rotor trailing edge.

Table 5. SDT cases chosen for validation.

Case #	Rotor	OGV	Operating Condition	Harmonic (× BPF)
1a	R4	NOM	Takeoff	1
1b	R4	NOM	Takeoff	2
2b	R4	NOM	Cutback	2
3b	R4	NOM	Approach	2
4a	R4	LVC	Takeoff	1
4b	R4	LVC	Takeoff	2
5a	R4	LVC	Cutback	1
5b	R4	LVC	Cutback	2
6a	R4	LVC	Approach	1
6b	R4	LVC	Approach	2
7a	R4	LN	Takeoff	1
7b	R4	LN	Takeoff	2
8a	R4	LN	Cutback	1
8b	R4	LN	Cutback	2
9a	R4	LN	Approach	1
9b	R4	LN	Approach	2

between data and prediction are made for the radial profiles of the first and second blade passing harmonics of the wake. The magnitude (squared) and the phase of the harmonics are compared in Figs. 9 and 10. To assist in relating to the sound pressure and power levels, the $20 \times \log_{10}$ of the wake magnitudes are compared. For plotting purposes, the phase is projected onto the principal branch between $-\pi$ and $+\pi$.

It is interesting to see that even though the meanflow comparisons (see Fig. 7) show highest discrepancy at approach, the wake harmonics are in closest agreement with data for both magnitude and phase. At higher speeds, CFD overpredicts the radial phase gradient, suggesting an overprediction of the rotor exit swirl angle. This is consistent with the meanflow comparisons in Fig. 7, where the axial velocity is slightly underpredicted and the tangential velocity is slightly overpredicted. This could perhaps explain the overall over-prediction of the magnitude of wake harmonics because the rotor is turning the flow more in CFD than in experiment and is hence overloaded.

At cutback and takeoff speeds, remnants of the tip vortex can be seen in the wake harmonic profiles between 85 and 100% span. At these speeds, the vortex core is very tight and the streamwise velocity defect due to vortex loss is high, whereas at approach the vortex core diffuses and its effect on the velocity defect

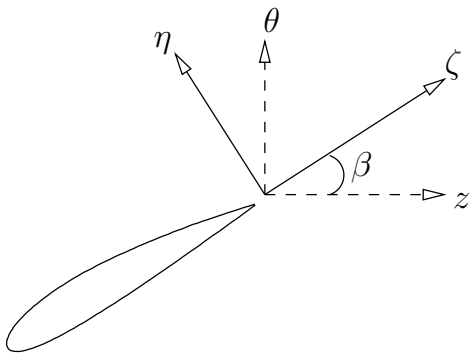

Figure 8. Definition of the co-ordinate systems used to define the rotor wake. ζ is the relative streamwise direction.

cannot be seen above the viscous wake defect.

Despite the sometimes significant differences between data and predictions for wake harmonics, the CFD predicted wake profiles are used for the remainder of the process to establish the accuracy of the prediction process.

2. Comparisons Against Rotating Rake Data

In the SDT, rotating rake measurements were made at both the inlet and the exhaust of the duct to not only measure the total fan tone noise power but to also identify the power distribution between different duct modes. The duct modes (basis functions) were chosen to be the Fourier-Bessel modes associated with a uniform (plug) flow in an annular/cylindrical duct for exhaust/inlet measurements.

The forward radiated acoustic waves pass through the rotor and hence only a portion of the total acoustic energy may get transmitted. Also the energy in the transmitted acoustic waves is scattered into different temporal and spatial (circumferential) modes. In order to accurately predict the inlet measured fan tones, the acoustic transmission through the rotor needs to be solved in addition to the forced response calculation of wake interaction with the stators. This problem is deferred for later and the current research is focused on the exhaust radiated noise. Any reflections from the rotors then transmitting through the stators and contributing to the exhaust noise radiation are currently ignored.

The non-reflecting boundary condition described in detail in reference[1] is used to decompose the outgoing acoustic power into a subset of duct modes. The flow behind the stators may not be radially uniform and may not always be completely axial. The duct modes for non-uniform flow are also not strictly orthogonal, however they are assumed to be close to orthogonal and any energy in the cross terms is ignored. The non-reflecting boundary condition implementation is borrowed as-is from the inviscid approach and no additional treatment is given when the linearized RANS equations are solved. This boundary condition was found to be stable for all the cases tested.

Figures 11, 12, and 13 compare the measured exhaust acoustic mode power levels against both viscous (VFTN) and inviscid (IFTN) prediction approaches. In general, both approaches overpredict the sound power, with the viscous approach showing larger deviation from data. The cases where the difference between the two approaches is large (over 5 dB), the main reason for the difference was identified to be in the wake specification step. In IFTN process, the wake was "idealized" to conform to the inviscid approach – this procedure led to artificial removal of vortical energy from the wake harmonic. Ironically however, that led to a closer match with the data.

The largest error in the VFTN process was found to be for the second blade passing harmonic at the approach condition. This is consistent for all OGV geometries and suggests that the primary reason is the overprediction of wake harmonic amplitude. While this can be clearly seen in Fig. 10 (a), the overprediction in wake harmonic magnitude is observed for the cutback and takeoff conditions as well. The main difference for the approach condition is at roughly 75% span, the CFD results show a noticable increase in vortical energy, whereas the data does not show this behavior. When the linearized RANS solution is carried out, this gust interaction with the OGV dominates the noise production. Perhaps the large discrepancy in the meanflow for this condition (indicating differences in rotor incidence) could explain the difference. The tip clearance also plays a big role in determining the strength of the tip gust and there could be geometric (tip clearance) differences between the CFD model and the experiment.

Another critical factor that determines the efficiency of noise generation is the radial gradient of the phase of the gust (wake harmonic), $arg(v'_\zeta)$. Figures 9 and 10 show that the radial phase gradient is over-predicted for the cutback and takeoff conditions for both first and second blade passing harmonics. A larger radial phase gradient typically reduces the interaction noise, due to the reduction in the portion of the span of the OGV that responds in phase. The large phase gradient partially offsets the noise over-prediction due to the over-predicted gust magnitudes for these two speeds. The radial phase gradient for the approach condition however is in close agreement with the data and hence the gust magnitudes appear more over-predicted than at other speeds.

Overall, the proposed prediction approach captures the dominant duct modes generated due to fan-OGV interaction although the sound power levels are generally overpredicted.

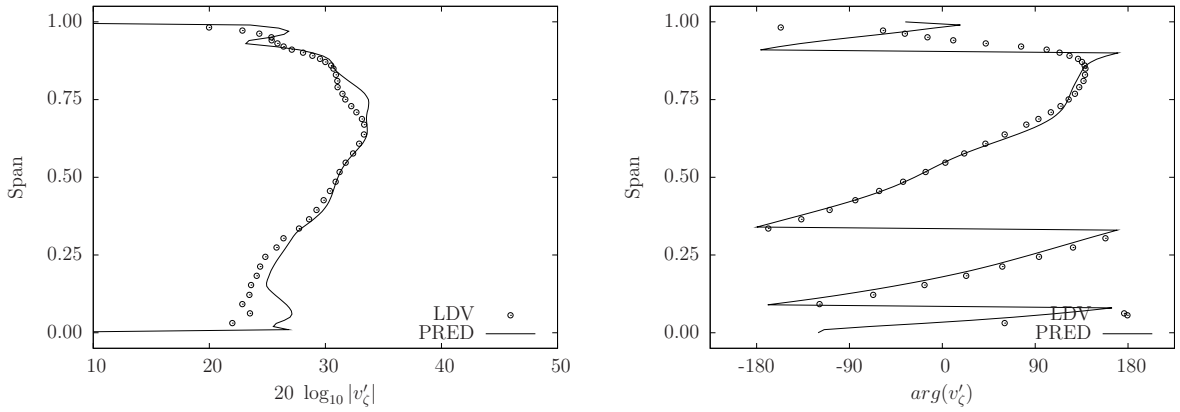

(a) Approach

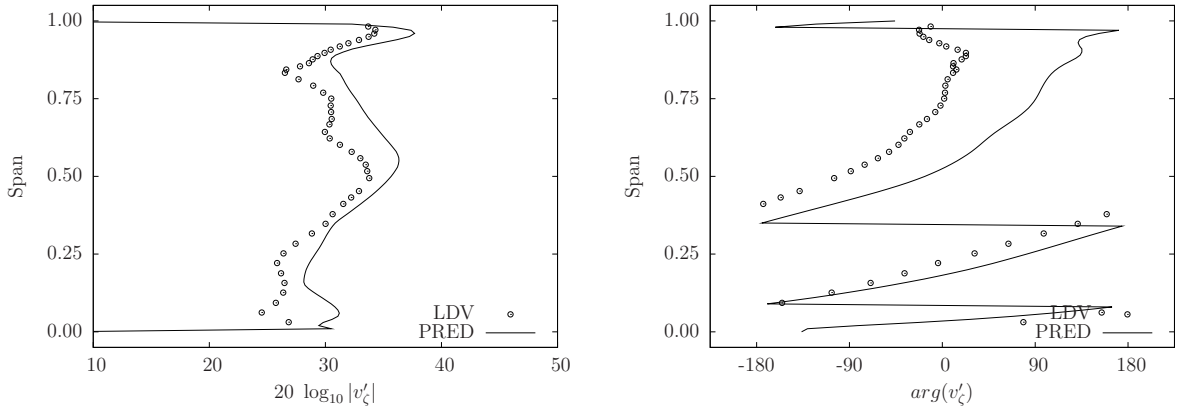

(b) Cutback

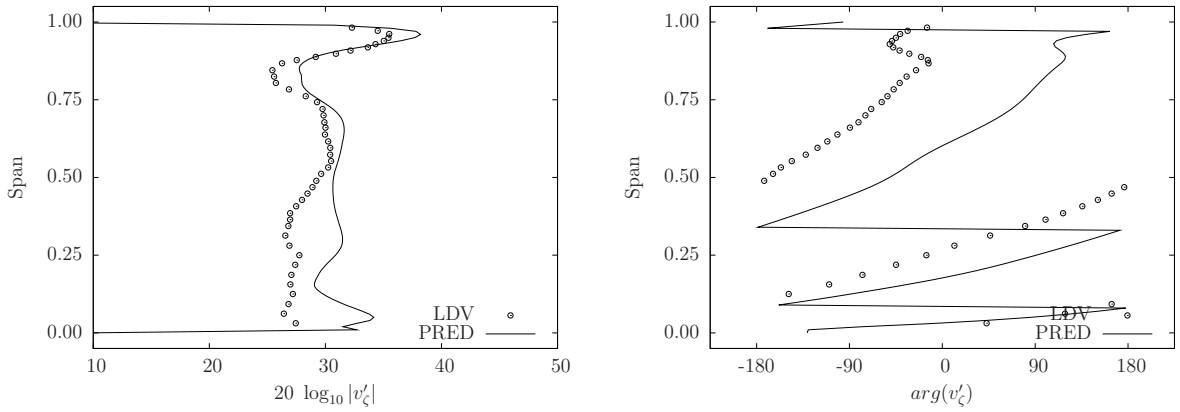

(c) Takeoff

Figure 9. Comparison of predicted versus measured first blade passing harmonic of the blade wake (streamwise velocity component, v_ζ) at an axial distance of 0.81 rotor tip chord downstream of rotor trailing edge.

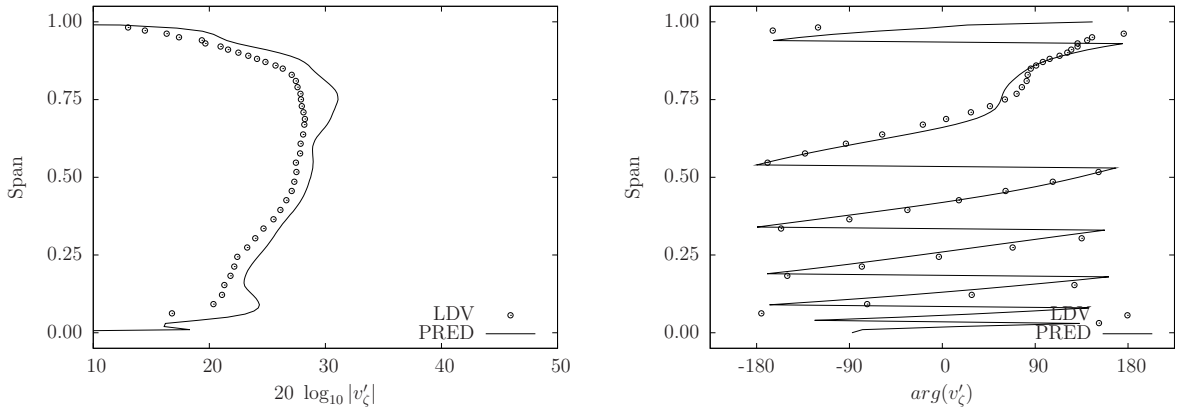

(a) Approach

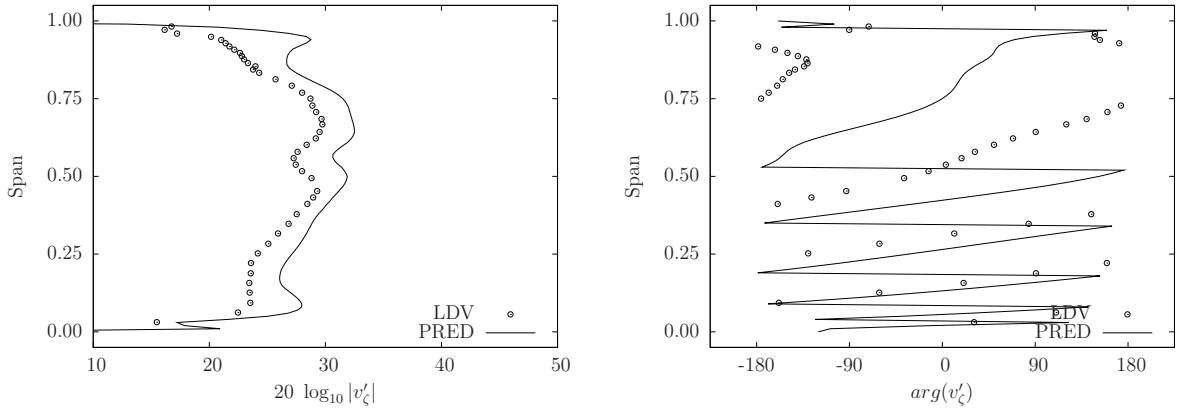

(b) Cutback

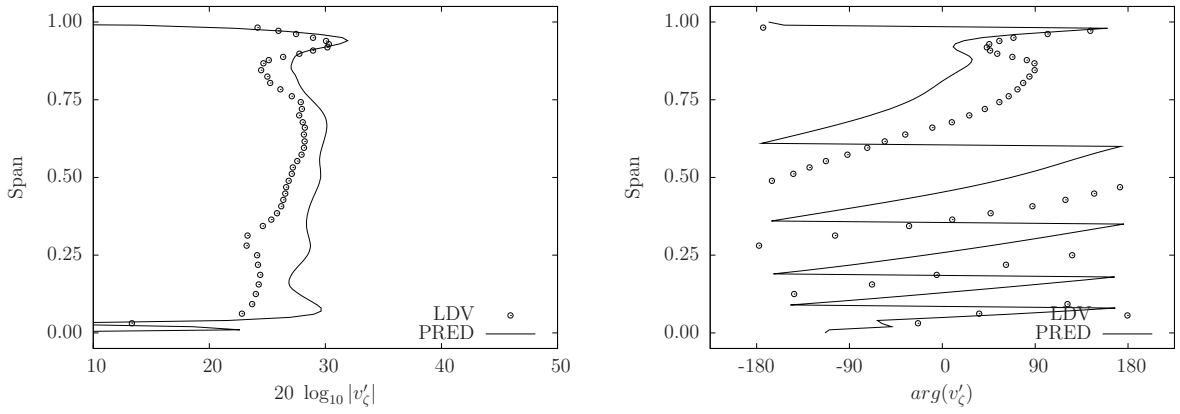

(c) Takeoff

Figure 10. Comparison of predicted versus measured second blade passing harmonic of the blade wake (streamwise velocity component, v_ζ) at an axial distance of 0.81 rotor tip chord downstream of rotor trailing edge.

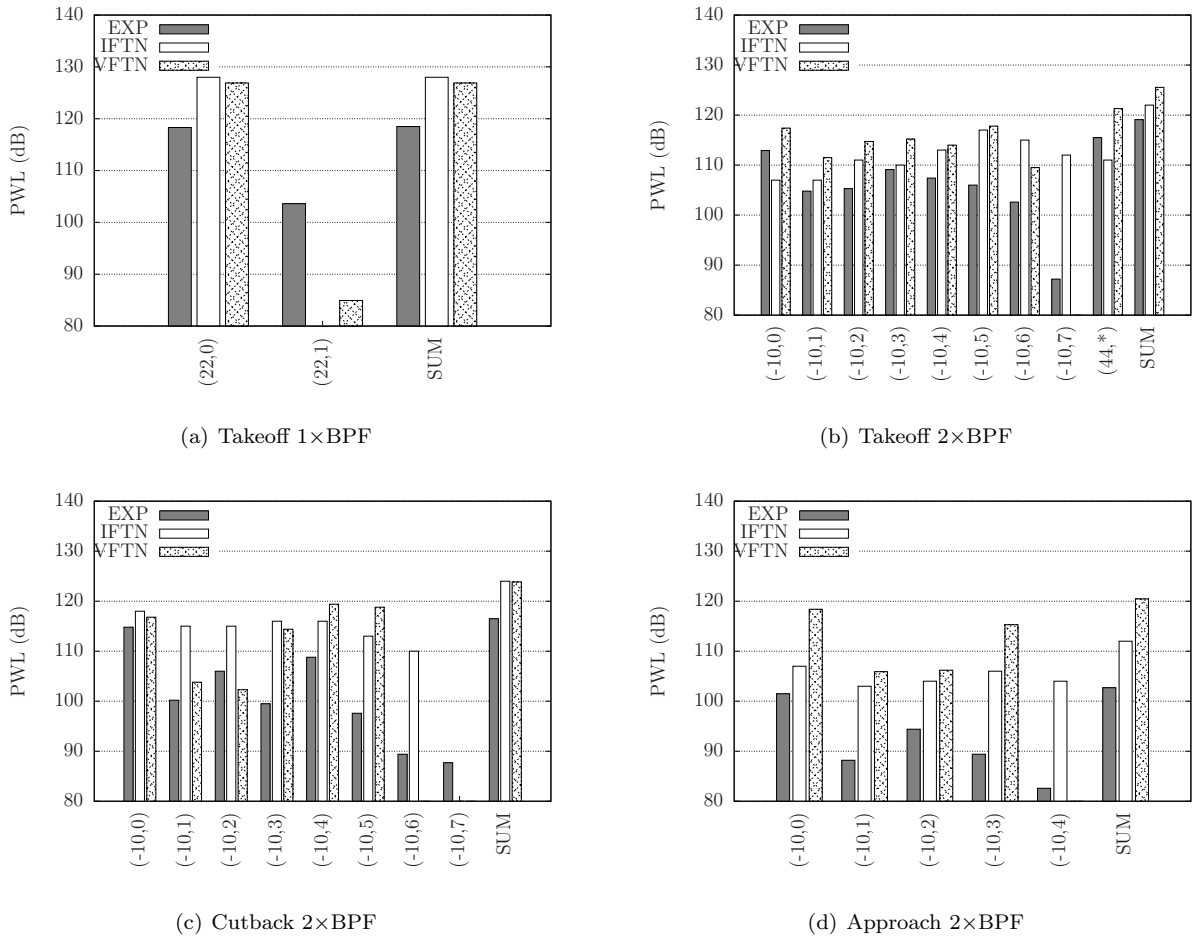

(a) Takeoff 1×BPF

(b) Takeoff 2×BPF

(c) Cutback 2×BPF

(d) Approach 2×BPF

Figure 11. Modal PWL results for the Nominal OGV configuration at Takeoff, Cutback, and Approach conditions.

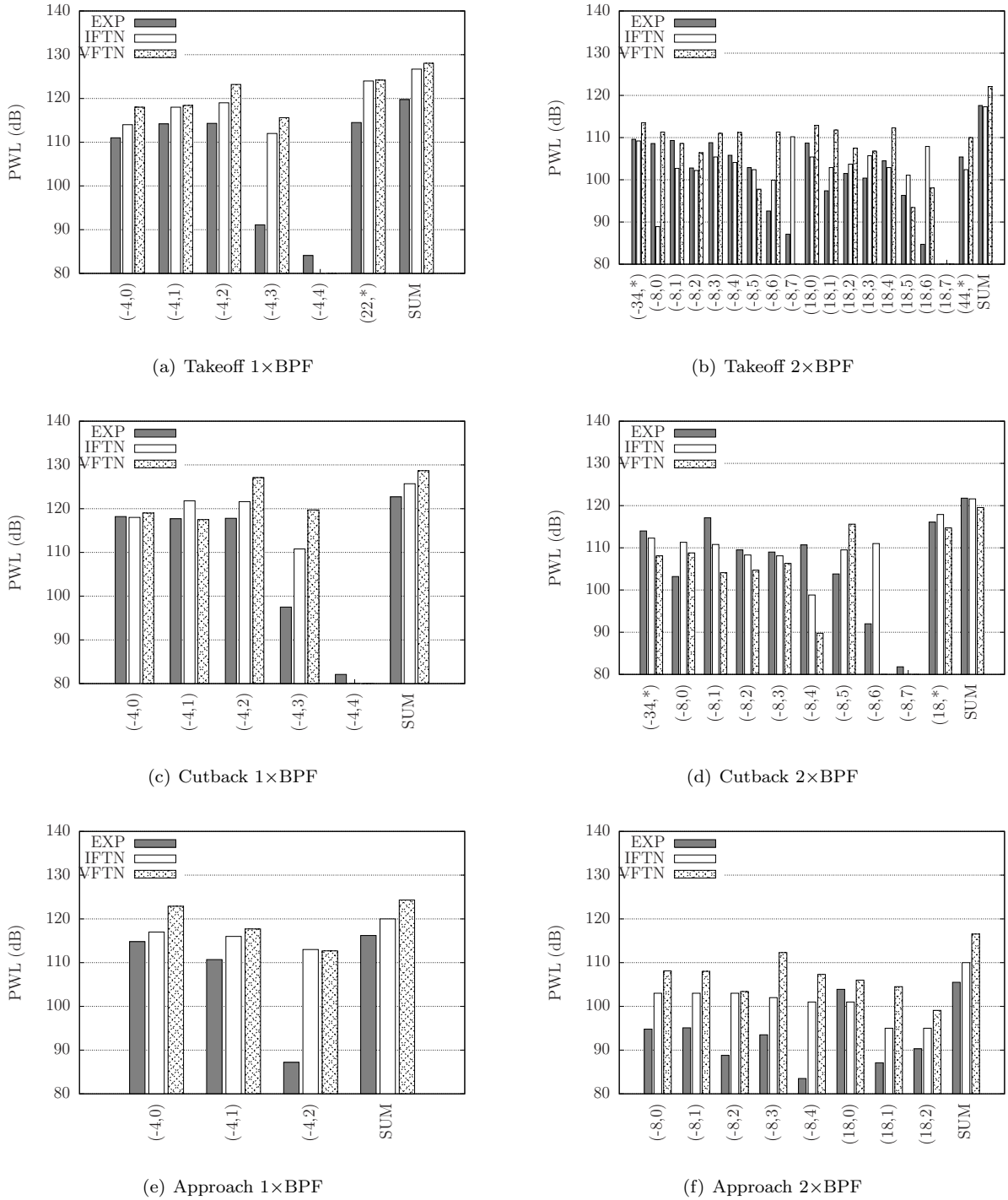

(a) Takeoff 1×BPF

(b) Takeoff 2×BPF

(c) Cutback 1×BPF

(d) Cutback 2×BPF

(e) Approach 1×BPF

(f) Approach 2×BPF

Figure 12. Modal PWL results for the Low Vane Count OGV configuration at Takeoff, Cutback, and Approach conditions.

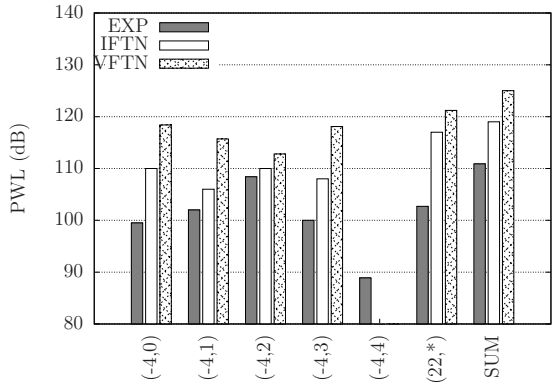

(a) Takeoff 1×BPF

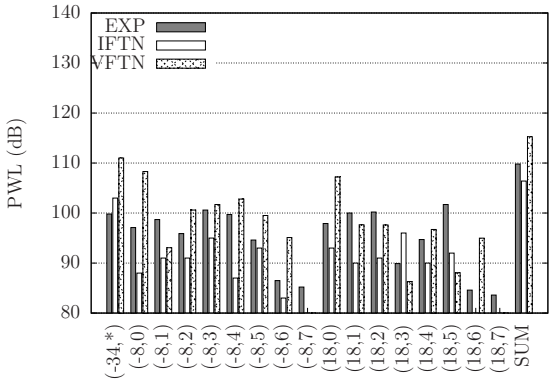

(b) Takeoff 2×BPF

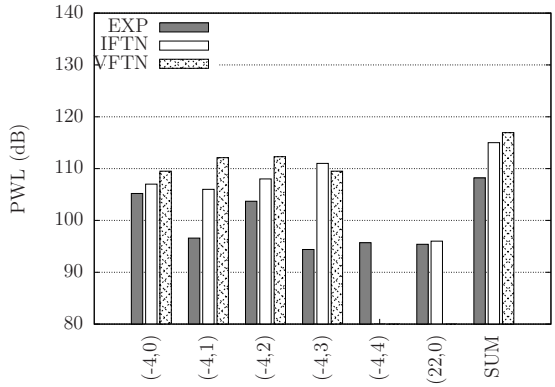

(c) Cutback 1×BPF

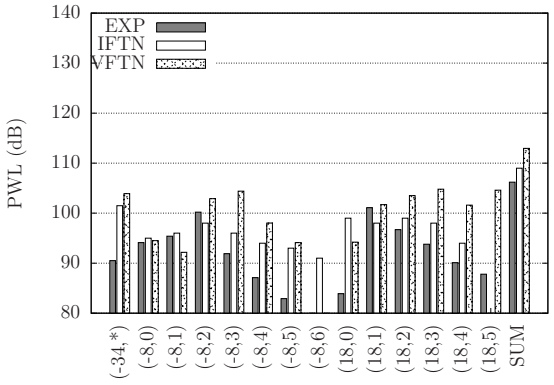

(d) Cutback 2×BPF

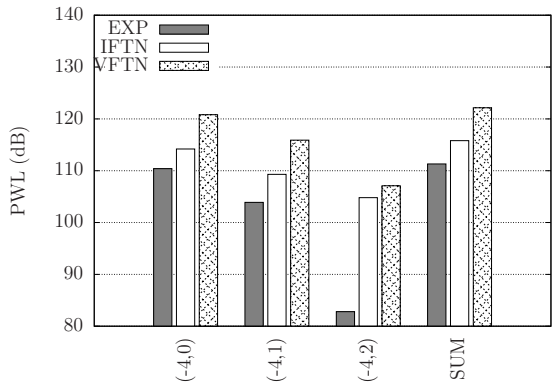

(e) Approach 1×BPF

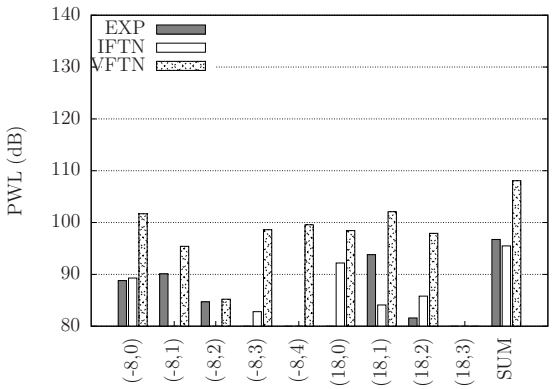

(f) Approach 2×BPF

Figure 13. Modal PWL results for the Low Noise OGV configuration at Takeoff, Cutback, and Approach conditions.

3. Geometric Trends Comparison

While absolute comparisons with data are ultimately desirable, geometric trend predictions are of particular interest for aeroacoustic design capability. In the SDT, there are two geometric trends: (1) effect of sweep (from LVC to LN), and (2) effect of reduced number of vanes (from NOM to LVC). Figure 14 compares the geometric trends between experiments and predictions (both IFTN and VFTN) at takeoff, cutback, and approach conditions. Comparison is made for individual harmonics as well as the total (sum of first and second blade passing harmonics) exhaust noise levels.

The benefit of sweeping the OGV in the downstream direction in reducing interaction noise is well known.[9,10] Sweeping the OGV back not only allows for additional wake mixing time (which reduces wake harmonic amplitudes), but also introduces additional radial phase gradient. The benefit of OGV sweep can be seen clearly in Fig. 14 on trend lines from LVC to LN. The effect is well captured by the VFTN process for cutback and approach speeds; at the takeoff condition, the benefit of sweep is slightly under-predicted.

The effect of vane count is confounded by the fact that the blade chord changes with the number of vanes to maintain the solidity (for aerodynamic similarity). Variation in chord changes the reduced frequency of the disturbance and hence the noise generated. The number of vanes also determines the circumferential modes generated and is a critical design parameter often used to cut-off the first blade passing frequency tone.

In the SDT, the NOM vane was designed to have the first blade passing frequency cut-off, while the LVC and LN designs are cut-on. The effect of this on overall noise can be seen in Figure 14 (f,i). The large increase in noise from NOM to LVC is due to the first BPF tone which is only present for the LVC geometry. It is important to note however that the vane count reduction significantly reduces the rotor-stator interaction broadband noise.[12]

IV. Concluding Remarks

A linearized RANS-based methodology for predicting rotor-stator interaction tones has been described. The approach improves upon a previously described prediction process[1] based on linearized Euler computations by removing inconsistent and ambiguous procedural elements. The proposed approach has been validated against canonical cases where the agreement with semi-analytical results is found to be very good. A detailed comparison against the NASA Source Diagnostic Test data has been performed for rotor wake harmonics and in-duct exhaust noise levels. The results are also compared to the previously established linearized Euler prediction process. In general, the geometric trend prediction accuracy is similar to the previous process, while the absolute levels are slightly over-predicted.

V. Acknowledgment

The authors would like to thank GE Aviation for providing financial support to carry out this research, and for granting permission to publish the results presented here. Thanks are also due to Edmane Envia and Gary Podboy of NASA Glenn for providing the acoustic and LDV measurement data. The authors also gratefully acknowledge their colleagues - Trevor Wood (GE Research), Muni Majjigi, Dennis Lynch, and John Wojno (GE Aviation), for many fruitful discussions on the subject.

References

[1] A. Sharma, S. K. Richards, T. H. Wood, and C. M. Shieh, "Numerical Prediction of Exhaust Fan-Tone Noise from High-Bypass Aircraft Engine," *AIAA Journal*, Vol. 47, No. 12, 2009.

[2] M. Giles, "Nonreflecting Boundary Conditions for Euler Equation Calculations," *AIAA Journal*, Vol. 28, No. 12, 1990, pp. 2050–2058.

[3] "Third Computational Aeroacoustics (CAA) Workshop on Benchmark Problems," *NASA/CP–2000-209790*, 2000.

[4] "Fourth Computational Aeroacoustics (CAA) Workshop on Benchmark Problems," *NASA/CP–2004-212954*, 2004.

[5] D. Prasad and J. M. Verdon, "A Three-Dimensional Linearized Euler Analysis of Classical Wake/Stator Interactions: Validation and Unsteady Response Predictions," *International Journal of Aeroacoustics*, Vol. 1, No. 2, pp. 137–163.

[6] S. N. Smith, "Discrete Frequency Sound Generation in Axial Flow Turbomachines," *Aeronautical Research Council R & M*, Vol. 3709, 1973.

[7] Goldstein, M. E., *Aeroacoustics*, McGraw-Hill International Book Company, 1976.

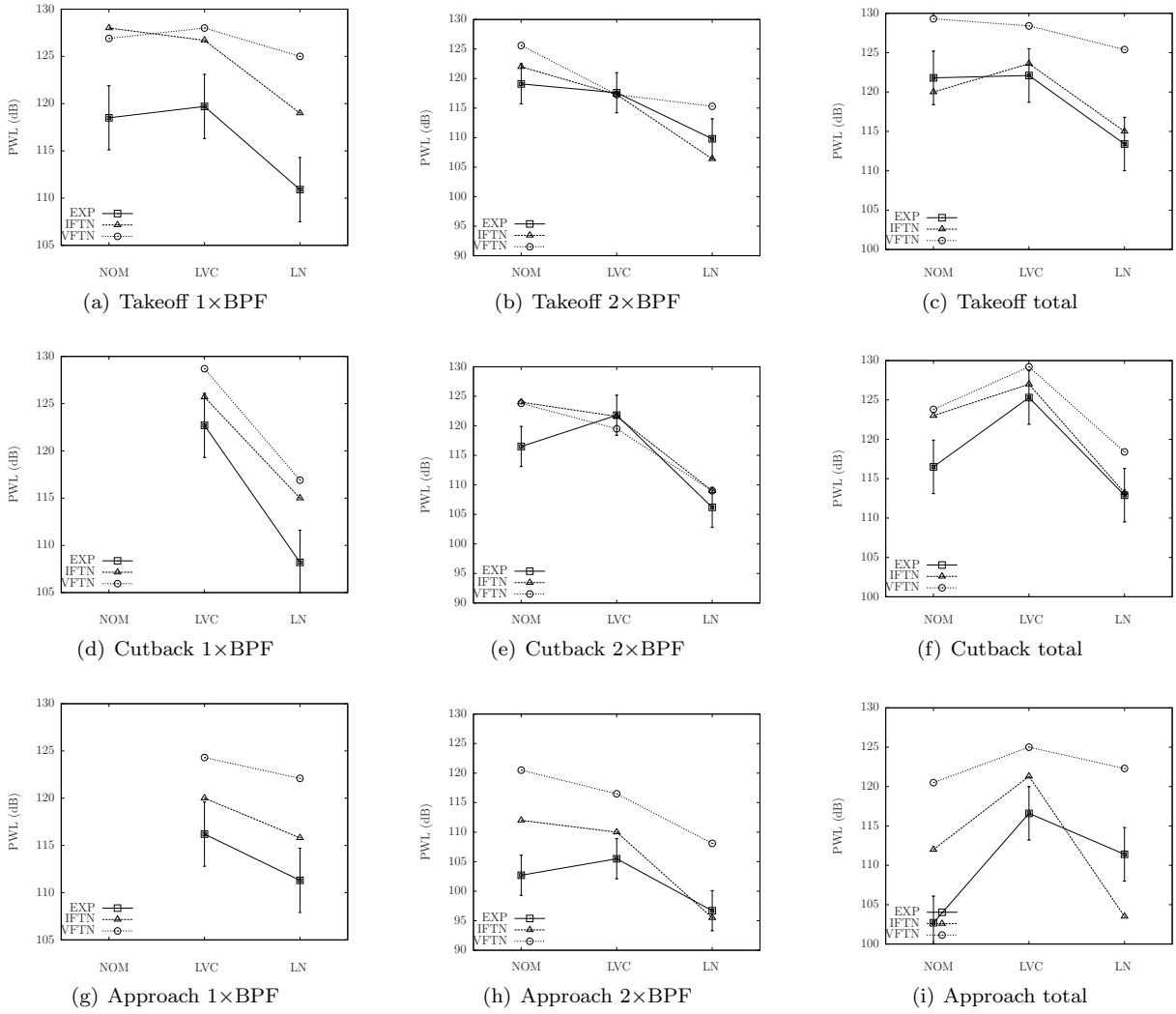

(a) Takeoff 1×BPF (b) Takeoff 2×BPF (c) Takeoff total

(d) Cutback 1×BPF (e) Cutback 2×BPF (f) Cutback total

(g) Approach 1×BPF (h) Approach 2×BPF (i) Approach total

Figure 14. Comparison of Geometry trends.

[8]M. Namba and J. B. H. M. Schulten, "Numerical Results of Lifting Surface Theory," *Third Computational Aeroacoustics Workshop on Benchmark Problems*, 2000, pp. 73–85.

[9]B. H. M. Schulten, "Vane Sweep Effects on Rotor/Stator Interaction Noise," *AIAA Journal*, Vol. 35, No. 6, 1997, pp. 945–951.

[10]R. Woodward, D. M. Elliot, C. E. Hughes, and J. J. Berton, "Benefits of Swept and Leaned Stators for Fan Noise Reduction," *NASA/TM 1998–208661*, 1998.

[11]W. R. Sears, "Some Aspects of Non-Stationary Airfoil Theory and Practical Applications," *Journal of Aeronautical Sciences*, Vol. 8, No. 3, 1941, pp. 104–188.

[12]Ganz, U. W., Joppa, P. D., Patten, T. J., and Scharp, D. F., "Boeing 18-Inch Fan Rig Broadband Noise Test," *NASA/CR-1998-208704*, 1998.